Wave Processes at Interfaces

Sigrid Andreae[1], Josef Ballmann[2], and Siegfried Müller[3]

[1] Lehr- und Forschungsgebiet für Mechanik der RWTH Aachen
sigrid.andreae@lufmech.rwth-aachen.de
[2] Lehr- und Forschungsgebiet für Mechanik der RWTH Aachen
ballmann@lufmech.rwth-aachen.de
[3] Institut für Geometrie und Praktische Mathematik, RWTH Aachen
mueller@igpm.rwth-aachen.de

Summary. We investigate the interaction of shock waves in a heavy gas with embedded light gas bubbles next to a rigid wall. This may give insight regarding cavitation processes in water. Due to the highly dynamical, unsteady processes under consideration we use an adaptive FV scheme for the computations to resolve accurately all physically relevant effects. The results are validated by comparison with tube experiments.

1 Introduction

The formation and collapse of vapor bubbles in a liquid is called cavitation. Lord Rayleigh discovered that pressure waves emitted during the process of cavitation [Ray17] may damage solids, e.g., marine screw propellers. Since then, the mechanism of cavitation damaging has been subject of experimental [Lau76, LH85] and analytical research. However, it is still unclear whether the shock and rarefaction waves or the liquid jet onto the solid is the main reason for the erosion of the material. The loading on an elastic-plastic solid exposed to shock and rarefaction waves in water was investigated by Specht in [ASB00]. Hanke and Ballmann showed one-dimensional results for a bubble collapse in water in [HB98].

Cavitation is induced by a pressure drop in the liquid below vapor pressure. Such a pressure decrease may occur due to local acceleration of the liquid flow caused by geometrical constraints, e.g., if the liquid flows through a narrow orifice or around an obstacle. In case the pressure drops below vapor pressure, the liquid bursts and creates a free surface filled with gas and vapor – the bubble. Due to changes in the flow field, the pressure in the liquid may increase afterwards causing the bubble to collapse. The collapse is accompanied by strong shock and rarefaction waves running into the bubble and the surrounding liquid. The shock wave focuses in the center of the bubble. This leads to extreme physical states in the interior. In addition, the shrinking of

the bubble leads to a compression of the vapor. Both effects evoke an increase of pressure which bulges the bubble. Hereby, a dynamic oscillation process is initiated which finally leads to the collapse of the bubble. If the collapse takes place next to a solid, the pressure distribution becomes asymmetric and a liquid jet develops [PL98] which is either directed towards or away from the solid boundary. The direction of the jet depends on the elasticity of the solid and on a ratio determined by the initial distance between the boundary and the center of the bubble divided by the maximum extension of the bubble. This has been shown experimentally by Brujan et al. in [BN$^+$01], [BN$^+$01a].

In order to investigate experimentally the dynamics of a bubble collapse, the bubble is produced by a laser pulse. Thereby, the fluid is heated in the focus of the laser and forms a small, hot gas bubble at very high temperature. This experimental setup provides an exact positioning of the bubble. The processes taking place in the interior of the collapsing and oscillating bubble and the prediction of onset and extent of the cavitation damaging are still subject of theoretical and experimental research. However, small time and space scales as well as the complicated dynamics make an experimental approach difficult. Therefore numerical investigations are needed to reveal information about the wave dynamics in the fluid as well as the damaging of the solid. Of particular interest are pressure contours and velocity vectors in the liquid phase as requested in [BN$^+$01a].

The primary objective of the present work is to provide an accurate prediction of all occurring wave phenomena. This concerns wave interactions among each other, with phase boundaries or neighboring solids. Besides, the occurrence of instabilities as, e.g., the Richtmyer-Meshkov instability. Since all present methods for simulating two-phase flows suffer from pressure oscillations at the phase boundary, we use a very dense and heavy gas instead of water . The occurring wave phenomena are expected to be qualitatively comparable with those in water.

For two-phase flow problems with different equations of state the phase boundary can be tracked or treated in a Lagrangian manner as a sharp, interior boundary using two meshes [Dick96]. The latter suffers from the drawback that the mesh has to be updated in every step which is expensive and time consuming and may result in a poor mesh quality for large displacements of the interface. Instead, we track the phase boundary using a level set method. Consequently, the phase boundary is represented as a mathematically sharp boundary as we will explain in Section 2. We do not implicate surface tension and mixing of the two fluids.

For the sake of completeness, it is to be mentioned that for a two phase flow of *one* fluid a homogenized approach is possible, as will be presented by Voß in [Vos02] and [Vos01]. There, one equation of state is used for the liquid as well as the gaseous phase and the so-called mixture region. Here, even states consisting of gas and vapor fractions can be modeled.

The small time scales of the unsteady problem require the numerical scheme to be highly efficient regarding computational time and memory re-

quirements. This is realized by a local grid refinement strategy. Furthermore, all physically relevant phenomena have to be reliably detected and adequately resolved. Moreover, the scheme has to be robust and must not exhibit numerical oscillations, e.g., pressure oscillations at the phase boundary. The details of the numerical scheme are presented in Section 3.

In Section 4 numerical results for a bubble collapse near a rigid wall are presented and the arising dynamic wave pattern is discussed.

2 Level Set

For modeling two-phase flows, there are mainly two different approaches to treat the two media, a fitting of the phase boundary with two separate grids connected by interface conditions, [Dick96], or one grid with a suitable algorithm to track the phase boundary. Since in the first case the grid has to be redesigned in every time step which is very time consuming, we use only one grid and the level set method to distinguish the two fluids.

The level set method, proposed by Osher and Sethian in [OS88], is a tool to track propagating interfaces without an explicit description like a function of the interface under consideration. Instead a scalar field given in the domain is used to represent the motion of the interface.

Consider the case of two domains Ω_1, Ω_2 separated by a contact surface Γ. Now, a scalar field $\phi = \phi(\mathbf{x}, t)$ is introduced which is $\phi(\mathbf{x}, t) < 0$ for $\mathbf{x} \in \Omega_1$ and $\phi(\mathbf{x}, t) > 0$ for $\mathbf{x} \in \Omega_2$, see Fig. 1. The interface Γ is evolved in time by the fluid velocity $\mathbf{v}$. Therefore, we may describe the time evolution of the scalar field ϕ by

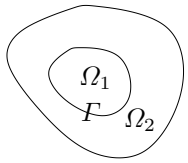

Fig. 1.

$$\frac{\partial \phi}{\partial t} + \mathbf{v} \cdot \nabla \phi = 0\,. \tag{1}$$

There are two different methods to exploit the evolution of the scalar field for tracking a moving interface. The most common approach suggested by Osher and Sethian in [Set96] is to define the scalar field as a smooth, signed distance function to the front under consideration, whereby the material interface corresponds to $\phi = 0$. Sussman et al. used this approach in computing incompressible two phase flows in [SSO94, SA$^+$99, SF99]. The smoothness of ϕ has to be sustained by a reinitialization after *each* time step. This way, it is guaranteed that the level set itself will not steepen and develop shocks. A disadvantage of this method is the loss of conservativity. Nguyen et al. suggested methods to recover the conservativity, see [NGF02].

Here, we follow an idea of Mulder et al. [MO92] where the level set function is not a smooth but a discontinuous scalar field. Initially, we assign $\phi(\mathbf{x}, t) = -1$ for $\mathbf{x} \in \Omega_1$ and $\phi(\mathbf{x}, t) = +1$ for $\mathbf{x} \in \Omega_2$. This notation for ϕ is sometimes called "color"-function. The sign (color) of ϕ decides which fluid

occupies which domain. Thereby, the choice of the equation of state is controlled. It has to be noticed that we track the jump in ϕ and not the zero level set.

Multiplying equation (1) with the density ϱ and employing the continuity equation of fluid dynamics yields a conservative form of the transport equation for ϕ, i.e.,

$$\frac{\partial \varrho\phi}{\partial t} + \nabla \cdot (\varrho\phi\mathbf{v}) = 0\,, \tag{2}$$

Written in this form equation (2) can be added to the system of conservation equations (1) as an additional equation. The main advantage of this approach is the preservation of conservativity.

3 Governing Equations and Method of Solution

The fluid flow is modeled by the time-dependent 2D Euler equations for compressible fluids. Appending the evolution equation (2) this leads to the system of conservation equations

$$\frac{\partial}{\partial t}\int_V \mathbf{U}\ dV + \oint_{\partial V} \mathbf{F}\cdot\mathbf{n}\ dS = 0 \quad \text{with} \tag{3}$$

$$\mathbf{U} = \begin{pmatrix} \varrho \\ \varrho\,\mathbf{v} \\ \varrho\,E \\ \varrho\,\phi \end{pmatrix}, \qquad \mathbf{F} = \begin{pmatrix} \varrho\,\mathbf{v} \\ \varrho\,\mathbf{v}\circ\mathbf{v} + p\mathbf{1} \\ \mathbf{v}\,(\varrho\,E + p) \\ \phi\,\mathbf{v} \end{pmatrix}.$$

Here, $\mathbf{U}$ is the array of the mean conserved quantities: density of mass, momentum, specific total energy and level set. p is the pressure and $\mathbf{v}$ the fluid velocity. The quantity V denotes a time-independent control volume with the boundary ∂V and the outer normal $\mathbf{n}$. The flux $\mathbf{F}$ contains only the convective terms. Since the two fluids under consideration are gaseous both, there is no need to deal with the surface tension at their contact surface.

The system of equations is closed by the perfect gas equations of state for both fluids $i = 1, 2$, i.e. the thermal equations, $p_i = R_i\,\varrho\,T$, and the caloric equations, $e_i = c_{\mathrm{v}i}\,T$. Herein, e_i is the internal energy and T the temperature. $c_{\mathrm{v}i}$ and R_i are the heat capacities at constant volume and the special gas-constants, respectively. Thereby, fluid $1, 2$ is present in $\Omega_1\,, \Omega_2$, respectively. The material properties, $c_{\mathrm{v}i}$ and R_i, are listed in Table 1. The evaluation of the equations of state is governed by the scalar field ϕ, i.e.,

$$p = \left\{ \begin{array}{lcl} p_1 & : & \phi < 0 \\ p_2 & : & \phi > 0 \end{array} \right\}. \tag{4}$$

The conservation equations (3) are discretized by a finite volume method. The convective fluxes are determined by solving quasi–one dimensional Riemann problems at the cell interfaces. For this purpose we employ a two-phase

Roe Riemann solver designed for the coupled system of the 2D Euler equations and the evolution equation (2) of the level set ϕ. For the construction of this solver we proceed similarly to [LV89] for real gases. In order to avoid non-physical expansion shocks we use Harten's entropy fix. The spatial accuracy is improved by applying a quasi one-dimensional second order ENO reconstruction. Due to the strong dynamic behavior of the considered flow problems the time integration is performed explicitly.

In order to properly resolve all physical relevant phenomena we need a very fine discretization of the computational domain. Due to the heterogeneity of the flow field, this high resolution is not needed throughout the entire computational domain but only locally near discontinuities. For this purpose we employ a dynamic local grid adaptation strategy to resolve the physically relevant phenomena at the expense of possibly few degrees of freedom and correspondingly reduced storage demands. The main distinction from previous work in this regard lies in the fact that we employ here recent *multi-resolution techniques*, see [Mül02].

The starting point is to transform the arrays of cell averages associated with any given finite volume discretization into a different format that reveals insight into the local behavior of the solution. The cell averages on a given highest level of resolution are represented as cell averages on some coarse level where the fine-scale information is encoded in arrays of *detail coefficients* of ascending resolution. This requires a *hierarchy of meshes*. The multiscale representation is used to create *locally refined meshes*. For details we refer to [Mül02].

Following Mulder [MO92] we chose ϕ as a color function in our computations. Mulder observed in [MO92] that using this formulation of ϕ the pressure shows spurious oscillations at the phase boundary. To reduce these oscillations we use averaged pressure and energy equations near the interface, i.e.,

$$p = \left\{ \begin{array}{ccc} p_1 & : & \phi < -\epsilon \\ (1-\alpha_\epsilon(\phi))\, p_1 + \alpha_\epsilon(\phi)\, p_2 & : & |\phi| < \epsilon \\ p_2 & : & \phi > \epsilon \end{array} \right\}, \tag{5}$$

$$e = T\, c_{\mathrm{v}} = T \left\{ \begin{array}{ccc} c_{\mathrm{v}1} & : & \phi < -\epsilon \\ (1-\alpha_\epsilon(\phi))\, c_{\mathrm{v}1} + \alpha_\epsilon(\phi)\, c_{\mathrm{v}2} & : & |\phi| < \epsilon \\ c_{\mathrm{v}2} & : & \phi > \epsilon \end{array} \right\}. \tag{6}$$

Here, the function $\alpha_\epsilon(\phi)$ is chosen as a linear interpolation between 0 and 1 in the interval $[-\epsilon, \epsilon]$, i.e., $\alpha_\epsilon(\phi) = (\phi/\epsilon + 1)/2$ for $|\phi| < \epsilon$. For our computations we chose $\epsilon = 0.5$. Results of a comparison between the approximate Riemann solver using this averaging method and an exact Riemann solver are given in Figs. 2(b) and 2(a). Since ϕ is initialized by $+1$ for fluid 1 and by -1 for fluid 2, ϵ has to be chosen less than 1 to make sure that the modification of the pressure law is only applied in the vicinity of the interface. Note that the initial jump of ϕ is smeared by the FV scheme. The width of this numerical transition layer depends on the underlying grid resolution. It becomes smaller with finer

grids. In particular, when the material boundary is a phase boundary and different equations of state have to be applied on both sides, a grid adaption strategy is strongly recommended to provide a high resolution of the interface.

From this point of view, equation (5) describes not really a physically relevant phase transition, it serves more as a numerical stabilizer of the phase boundary.

4 Numerical Results

The current work focuses on the ability of the scheme to accurately resolve the dynamics and wave pattern occurring in the presented test configurations for two-fluid flow. At first, we validate our scheme using experiments performed by Haas and Sturtevant, [HS87]. Herein, a shock runs across a bubble filled with helium in the one case and with R22 gas in the other. R22 is the heavy refrigerant chlorodifluromethane ($CHClF_2$). In Table 1 the physical properties of the gases under consideration are given. The surrounding fluid is air in both cases. We compare our numerical results with the schlieren photographs taken by Haas and Sturtevant. The third configuration is a helium bubble surrounded by R22 and placed next to a rigid wall, with initial conditions corresponding to an explosion problem. The main focus lies on the interaction of the emitted waves with the wall. Since we expect the occurring wave phenomena have something in common with the formation and collapse of a cavitation bubble, this configuration indicates possible causes for the damaging mechanisms accompanying cavitation in the related experiments. The

Table 1. Molecular weight u_{mol}, special gas-constant R, ratio of specific heats γ and speed of sound c (at 293.15 K, 101, 35 kPa) for air, helium and R22.

fluid	u_{mol} [10^3kg/mol]	R [J/kg/K]	γ	c [m/s]
air	28.964	287.0	1.4	343.3
helium	4.003	2077.0	1.66	1007.4
R22	864.687	96.138	1.178	184.0

characteristic physical quantity in dealing with wave interactions with boundaries is the *acoustic impedance* ϱc. Herein, c is the speed of sound. The ratio of the acoustic impedances of two fluids governs what happens to a shock wave traveling through fluid 1 and impinging on the phase boundary between fluid 1 and 2. According to the acoustic wave theory, the impinging shock wave is split up in a transmitted part traveling through Fluid 2 and a reflected part. The larger the jump of the acoustic impedance the more energy is reflected. In case, $(\varrho c)_1 >> (\varrho c)_2$ most of the energy is reflected with a phase change of 180°. If $(\varrho c)_1 << (\varrho c)_2$ most of the energy is reflected, too, but

without change of phase angle. The results for shock impacts on the helium and the R22 bubble presented in Section 4.2 show the influence of the acoustic impedance on the wave pattern. This will be discussed later in this chapter.

4.1 Validation

To validate the solver the solution of a 1D Riemann problem is compared to the exact solution, see Figure 2(a), evaluated with an exact Riemann solver by Colella and Glaz [CG85] which is capable to deal with two phases. Apart from some slight pressure wiggles at the phase boundary, our approximate solver gives satisfying results. For time $t = 0$ the membrane at $x = 0\,\mathrm{cm}$ bursts;

Table 2. Initial conditions for two phase Riemann problem with helium and R22.

	helium bubble	R22 surrounding
$\varrho\,[\mathrm{kg/m^3}]$	20.0	10.0
$p\,[\mathrm{N/m^2}]$	1.217×10^7	281684.3
$T\,[\mathrm{K}]$	293.0	293.00
$\varrho\,c\,[\mathrm{kg/s/m^2}]$	20101.85	1821.78
$v_x, v_y\,[\mathrm{m/s}]$	0.0 , 0.0	0.0 , 0.0

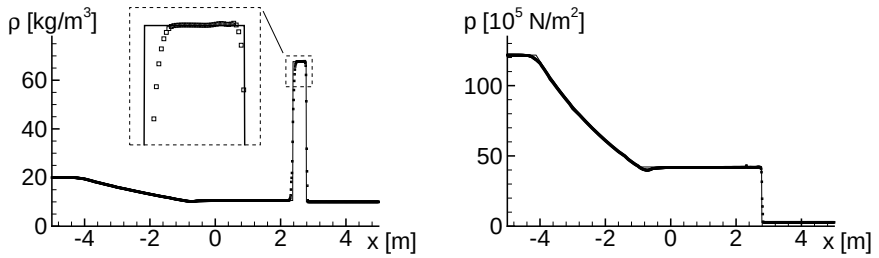

(a) (b)

Fig. 2. Exact and approximative solution for the two-phase Riemann problem helium (left) and R22 (right); density (a) and pressure (b).

on the left hand side in the high pressure region is helium, on the right hand

side R22. A shock runs into the low pressure region. Behind the shock the density jumps from $10\,\mathrm{kg/m^3}$ to $67.2107\,\mathrm{kg/m^3}$. The shock is followed by a very fast contact discontinuity. Over the contact discontinuity the density drops to $10.5365\mathrm{kg/m^3}$ which is nearly its right initial value. In the high pressure region runs a rarefaction wave.

4.2 Shock Bubble Interaction

Haas and Sturtevant performed experiments with shocks passing gas inhomogeneities of helium or R22 in an air surrounding to clarify the mechanisms of turbulence and mixing caused by shock waves, see [HS87]. They carried out two-dimensional and three dimensional experiments. In the two-dimensional experiments, we compare with a cylindrical volume is enclosed by a $0.5\,\mu$m thick nitrocellulose membrane which bursts under the impact of the shock wave. With shadowgraph photography wavefronts and the topology of the bubble were made visible.

The geometrical setup shown in Fig. 3 is the same for both problems. The initial mesh has 125×10 cells and 5 levels of refinement are used. Due to the mirror symmetry of the problem, only the upper half was computed. A shock coming from left impinges on a gas bubble. Initially, the bubble and the surrounding pre-shocked air are at rest and in thermal and mechanical equilibrium. Corresponding to the geometrical situation presented in Figure 3, the initial conditions for the problems discussed here are given in Tables 3 and 4.

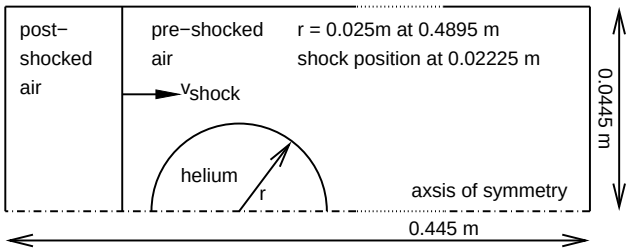

Fig. 3. Computational domain for 4.2.

Helium Bubble in Air

In the first computation the setup is the helium filled gas bubble surrounded by air. The initial conditions are given in Table 3 and the geometry in Fig. 3. Figure 4 shows the time evolution of the density gradient in the domain given in Figure 3. In Figures 5(a) and 5(b) the pressure p is plotted in z-direction over the x-y-plane and the phase boundary is marked as a black line. In the x-y-plane the pressure gradients are shown (shock fronts visible as black lines).

Table 3. Initial conditions for shock interaction with helium bubble.

	post-shocked air	pre-shocked helium	pre-shocked air
ϱ	1.376	0.138	1.0
p	1.575	1.0	1.0
$\varrho\, c$	1.742	0.479	1.183
v_x, v_y	0.396 , 0.0	0.0 , 0.0	0.0 , 0.0

These figures show the same instant as Figures 4(b) and 4(d). Figure 6 shows a comparison between the experimental and our computational results. Two clippings of the adapted mesh are shown in Figures 7(a) and 7(b).

In Figure 4(a) the incoming shock (marked as i) has already crossed the most left part of the bubble boundary. It is partly transmitted as a refracted shock (rr) and partly reflected as a rarefaction wave (rw). This behavior is governed by the ratio of the acoustic impedances, see values given in Table 3. Inside the bubble the transmitted shock runs ahead since the speed of sound in helium is higher than in air at the same temperature. The shock-front is curved due to the spherical shape of the undisturbed phase boundary. The fore-running shock in helium arches as a thin, black line from $x = 0.039\,\mathrm{m}$ to $x = 0.0315\,\mathrm{m}$ at the phase boundary where the shock just hits the boundary. Outside the bubble the incident shock is visible as a straight, black, vertical line. The density jump at the phase boundary is a thin, opaque line marked as (pb). Behind of the shock, the reflected rarefaction wave appears as a dark area. Since in the very beginning of the shock bubble interaction the shock front is parallel to the phase boundary, all the waves travel in x-direction. Later on, the shock impinges on the phase boundary under an increasing angle, see Fig. 4(b). Due to the laws of geometrical optic the rarefaction wave is reflected under the same angle as the shock impinges on the helium surface. Since the shock inside is faster than outside, a shock wave (marked s as " side" shock) emanates where the refracted shock meets the phase boundary. A complicated four shock configuration develops which Henderson explained in [HCP91] and called twin regular reflection refraction. In Figure 4(c) the refracted shock is just passing the most right boundary of the bubble at $x = 0.073\,\mathrm{m}$, whereas the incident shock is at $x = 0.043\,\mathrm{m}$. The acoustic impedance in the post-shocked helium is only $0.542\,\mathrm{kg/m^2/s}$ but in the pre-shocked air $1.183\,\mathrm{kg/m^2/s}$. Therefore, the air acts in the sense of a rigid boundary which makes that the reflected part of the shock wave hitting this boundary is a shock. This reflected shock (rl) focuses on the x-axis at $0.059\,\mathrm{m}$ which is visible as a small, light dot in the density gradients of Fig. 4(d) (marked by an arrow). The focus is more distinct in the corresponding pressure gradients, see Fig. 5(b). Here, the pressure is plotted in z-direction over the x-y-plane. Below, in the same figure which itself shows the pressure gradient isolines shown in gray-scale. As a result of the higher shock speed the helium near the x-axis is stronger accelerated than the air above it. Thereby, an anti-clockwise

rotation of the bubble content is induced and at the symmetry axis the bubble constricts and develops a small throat. The helium volume remains rotating, splits up at the x-axis and travels circulating upstream, see Figs. 4(h)–4(j).

We compared our results to photographs taken by Haas and Sturtevant, see [HS87], and found a good agreement see Figs. 6. In particular, the numerical results exhibit all waves visible in the schlieren photographs. However, since the numerical results do neither include the complete experimental setup, e.g., the support for cylindrical membrane in Fig. 6(c), nor perturbations due to the rupture of the membrane, the comparison can only be qualitatively. Nevertheless, as indicated by the same labels as in Fig. 4 all the waves from the experiment are resolved in the computation. In particular, the topology of the bubble is excellently reproduced. Notice that the ring which was necessary to fix the bubble in the experiment must not be confused with a wave surface.

To show qualitatively the grid refinement, a part of the adapted mesh is presented in Fig. 7(a). The shock at $x = 0.27\,\mathrm{m}$ as well as the bubble contour are well resolved. The re-coarsening of the grid inside the bubble is visible in Fig. 7(b).

R22 Bubble in Air

Table 4. Initial conditions for shock interaction with R22 bubble.

	post-shocked air	pre-shocked R22	pre-shocked air
γ	1.4	1.178	1.4
ϱ	1.376	2.985	1.0
p	1.575	1.0	1.0
$\varrho\, c$	1.742	1.875	1.183
v_x, v_y	0.396 , 0.0	0.0 , 0.0	0.0 , 0.0

For the case of an R22 bubble in air, physical data is given in Table 4. The density gradients corresponding to the experimental schlieren images are shown in Fig. 8. Figure 11 shows the absolute value of the velocity and integral-curves of the instantaneous velocity field. In Figure 9(a) the density is plotted in z-direction over the x-y-plane. In the x-y-plane the density gradients isolines are plotted in gray-scale; Figure 9(b) shows a similar plot for the pressure in z-direction, but here the phase boundary is marked with a black line, and in the x-y-plane the pressure gradient isolines are presented.

Since the acoustic impedance of R22 is only slightly higher than the acoustic impedance for the post-shocked air, see Table 4, the incident shock (i) is mainly transmitted and only a small portion is reflected as a shock (rl), see Fig. 9(a). There, the transmitted and thereby refracted shock (rr) is visible as a concave curved black line extending from $x = 0.037\,\mathrm{m}$ to $x = 0.048\,\mathrm{m}$.

Compared to the incident shock (i) the refracted shock (rr) is slower, because the sound speed in R22 is lower than in air. This is also the reason for the higher acceleration of the air above the bubble compared to that of the gas R22. This fact leads to a clock-wise rotation of the material in the R22 bubble later on. The outward running shock diffracts since it is decelerated at the phase boundary, see Fig. 8(c). Between the incident shock (i) and the inside running shock (rr) develops a compression wave (cw). By the compression wave the flow direction is turned by 90° towards the symmetry axis as indicated in Fig. 11. The front of the refracted shock bends more and more until it focuses on the x-axis at the phase boundary, see box on left side in Fig. 8(e). The arising pressure peak is depicted in Fig. 9(b). The shock is reflected after focusing and runs outward, see wave (rf) in Fig. 8(f). Again the shock (rf) is traveling slower in the R22 than in the helium. When the incident shock has passed the bubble it crosses its symmetric counterpart, see Fig. 8(f) at $x = 0.06\,\mathrm{m}$. Thereby, a reflected shock (s) running upstream is induced. These two shocks (s and rf) pass across the bubble in upstream direction and cause reflected and refracted waves inside the R22 bubble visible in the density gradients of Figs. 8(g)–8(i). Since they do not produce new physical effects they are not discussed further. The bubble migrates downstream and thereby it prolongates and rolls up its top (t). In Figure 8(j) the phase boundary represented by the zero level $\phi = 0$ is indicated by a solid, black line. Obviously, there are growing instabilities on the top of the structure. It is assumed that these are Rayleigh-Taylor instabilities due to the shock passing across a curved phase boundary.

The comparison with the experiment is given in Fig. 10. Again, the ring from the experimental setup is visible. The wave (w) at the bottom of Fig. 10(c) is a reflection from the shock tube wall. A good agreement between the phase boundaries (pb), the incident and refracted shocks (i and rr) is visible in in Figs. 10(a) and 10(c). Note that even the compression wave (cw) is resolved. In Figures 10(b) and 10(d) the phase boundary (pb) as well as the shock (rf) – reflected from the focus of the refracted shock – match perfectly their experimental counterparts. At the left border the reflected shock (s) from the crossing of the incident shocks at the symmetry axis is visible.

4.3 Explosion Problem Helium in R22 Next to a Rigid Wall

This computation is motivated by the idea of a laser induced vapor bubble in a liquid next to a rigid surface. The resulting bubble expands very fast and causes a pressure wave in the liquid which interacts with the wall and after reflection again with the bubble. In the case discussed in the sequel, we study the sudden expansion of a hot, high pressure helium bubble with cylindrical shape surrounded by the heavy gas R22 at low temperature. The midpoint of the bubble of diameter 0.01 m is placed at $x = 0.14\,\mathrm{m}\,, y = 0.08\,\mathrm{m}$ at the right of the computational domain which has the size $0.16\,\mathrm{m} \times 0.32\,\mathrm{m}$. Since

the problem is mirror-symmetric with respect to the x-axis we computed only the upper half.

Both fluids are treated as perfect gases. The chemical data is given in Table 1. The zero level set lies on the phase boundary between helium and R22; it is indicated as a white, dashed line in the Figs. 12–17. The initial conditions correspond to a the two-phase Riemann problem in Section 4.1.

The computational results for the two-dimensional explosion problem are presented in Figures 12–21. The series of Figs. 12–17 show pressure (a), density (b) and the corresponding grid (c) at different times. The phase-boundary which is evaluated from the level set function as its zero level is indicated as a white dashed line in every picture. In the very beginning a circular shock wave runs undisturbed outward, see Figs. 12(a) and 12(b). It is closely followed by the contact discontinuity (white dashed line). Inwardly, a rarefaction wave runs concentrically into the center of the bubble. There, it is reflected as a now outwards running rarefaction wave which follows the shock and the contact discontinuity, see Figs. 13(a) and 13(b). In Figures 12(c) and 13(c) it is clearly visible that the mesh is refined close to the waves and is re-coarsened in the center after the reflection of the rarefaction wave. The first wave hitting the rigid wall is the shock. It is then reflected as a shock wave and its pressure level increases due to the superposition, see pressure and density legend in Fig. 13. The reflected shock passes over the contact discontinuity which is decelerates thereby. Due to the high pressure region behind the shock, the contact discontinuity does not reach the wall, but is repelled from it, see Fig. 21(a) at $20\,\mu$s. The outward running waves set the material inside the bubble in an outward directed motion, see Fig. 18, and a shock develops at time $t = 29\,\mu$s, see Fig. 14(a) and Fig. 21(a) at $x = 0.13\,$m and $x = 0.15\,$m, respectively. However, the reflected rarefaction wave decelerates as well as the inward running rarefaction wave induces an outward directed velocity field which decelerates this shock so that the shock becomes nearly stationary. The shock that was reflected at the solid wall overtakes the shock and due to their interaction a small contact discontinuity appears, see Fig. 21(b) at $x = 0.147\,$m and $t = 35\,\mu$s. In theses pictures, the wave dynamics on the x-axis in a range from $x = 0.08 - 0.16\,$m are plotted as pressure (Fig. 21(a)) and density (Fig. 21(b)) isolines in an x-t plane.

Later on, the shock reflected from the wall also interacts with the rest of the shock in the interior of the helium bubble. They cross each other mainly undisturbed and a contact discontinuity emerges from the interaction, see $x = 0.137\,$m in Fig. 21(a) (the phase boundary is marked as a black, dotted line). Since the initial shock front is spherical, it hits the wall under a continuously increasing angle. At first, the shock impinges onto the wall under an angle of $0°$ and is reflected regularly. With increasing angle, however, a regular reflection becomes impossible as explained by, e.g., Ben-Dor in [BD91] and a Mach stem develops, see Fig. 17 on the x-axis at $y = 0.072\,$m. The slip line (sl) coming from the Mach stem (ms) is visible in Fig. 19. In the case of a cavitation bubble in water the Mach stem of the reflected shock produces surface waves

in the wall which could be one reason for cavitation damaging. The pressure distribution at the rigid wall in Fig. 20 displays the loading jump evoked by the Mach stem – visible at $y = 0.0517\,\mathrm{m}$ – on the solid.

5 Conclusion and Future Work

We presented results for highly dynamical two-fluid flow problems with wave interactions at material boundaries. The comparison with experiments in Section 4.2 verifies that our solver is adequate for computing two-fluid flow problems for different perfect gases. The advanced grid refinement strategy automatically detects all appearing waves and provides a perfect resolution of those waves. For the test case of an exploding gas bubble next to a rigid wall, the complicated wave interactions are well resolved and give hope for further computations with gas and liquid.

6 Acknowledgment

The authors would like to thank Dipl.-Math. Alexander Voß, Institut für Geometrie und Praktische Mathematik, RWTH Aachen, for helpful discussions on Riemann problems and programming issues. In particular, the discussions on the physical modeling have been very helpful. This work was financially supported by the DFG Priority Research Program "Analysis and Numerics for Conservation Laws".

References

[ASB00] Andreae, A., Specht, U., Ballmann, J.:Wave phenomena at liquid-solid interfaces. In: Proceedings of Eighth International Conference on Hyperbolic Problems - Magdeburg,Birkhäuser (2000)

[BD91] Ben-Dor, G.: Shock Wave Reflection Phenomena. Springer (1991)

[BN+01] Brujan, E.-A., Nahen, K., Schmidt, P., Vogel, A.: Dynamics of laser-induced cavitation bubbles near an elastic boundary. J. Fluid Mech., **433**, 251–281 (2001)

[BN+01a] Brujan, E.-A., Nahen, K., Schmidt, P., Vogel, A.: Dynamics of laser-induced cavitation bubbles near elastic boundaries: influence of the elastic modulus. J. Fluid Mech., **433**, 283–314 (2001)

[CG85] Colella, Ph., Glaz, H. M.: Efficient solution algorithms for the Riemann problem for real gases. J. Comp. Phys., **59**, 264–289 (1985)

[Dick96] Dickopp, Ch.: Ein Navier Stokes Löser zur Simulation kollabierender Kavitationsblasen in der Nähe elastischer Festkörperoberflächen. Shaker Verlag, Aachen (1996)

[HS87] Haas, J. F., Sturtevant, B.: Interaction of weak shock waves with cylindrical and spherical gas inhomogeneities. J. Fluid Mech., **181**, 41–76 (1987)

[HB98] Hanke, M., Ballmann, J: Strong changes of state in collapsing bubbles. ZAMM, **78**, 453–453. (1998)

[HCP91] Henderson, L. F., Colella, P., Puckett, E. G.: On the refraction of shock waves at a slow-fest gas interface. J. Fluid Mech., **224**, 1–27 (1991)

[Lau76] Lauterborn, W.: Numerical Investigation of Nonlinear Oscillations of Gas Bubbles in Liquids. J. Acoust. Soc. Am., **59** 2,283–293 (1976)

[LH85] Lauterborn, W., Hentschel, W.: Cavitation bubble dynamics studied by high speed photography and holography: Part One. Ultrasonics, **23**, 260–268 (1985)

[LV89] Liu, Y., Vinokur, M.: Nonequilibrium flow computations. I. An analysis of numerical formulations of conservation laws. J. Comp. Phys., **83**, 373–397 (1989)

[MO92] Mulder, W., Osher, S.: Computing interface motion in compressible gas dynamics. J. Comput. Phys., **100**, 209–228 (1992)

[Mül02] Müller, S.: Adaptive Multiscale Schemes for Conservation Laws. Accepted for publication in Lecture Notes on Computational Sciences and Engineering. Springer (2002)

[NGF02] Nguyen, D., Gibou, F., Fedkiw, R.: A fully conservative ghost fluid method & stiff detonation waves. 12th Int. Detonation Symposium, San Diego, CA (2002)

[OS88] Osher, S., Sethian, J. A.: Fronts Propagating with Curvature-Dependent Speed: Algorithms Based on Hamilton-Jacobi Formulations. J. Comput. Phys.,**79**, 12–49 (1988)

[PL98] Philipp, A., Lauterborn, W.: Cavitation erosion by single laser-produced bubbles. J. Fluid Mech., **361**, 75–116 (1998)

[Ray17] Lord Rayleigh: On the pressure developed in a liquid during the collapse of a spherical cavity. Phil. Mag., **34**, 94–98 (1917)

[Set96] Sethian, J. A.: Level Set Methods, Cambridge Monographs on Applied and Computational Mathematics (1996)

[SSO94] Sussman, M.,Smereka, P., Osher, S.: A Level Set Approach for Computing Solutions to Incompressible Two-Phase Flow. J. Comput. Phys.,**114**, 146–159 (1994)

[SA+99] Sussman, M., Almgren, A. S., Bell, J. B., Colella, P., Howell, L. H., Welcome, M. L.: An Adaptive Level Set Approach for Incompressible Two-Phase Flows. J. Comput. Phys., **148**,81–124 (1999)

[SF99] Sussman, M., Fatemi, E.: An efficient, interface-preserving Level Set Redistancing Algorithm and its Application to interfacial incompressible Fluid Flow. SIAM J. Sci. Comput.,**20**/4, 1165–1191 (1999)

[Vos01] Voß, A.: A Numerical Library for Fluids and Convex and Nonconvex EOS Including Phase Transition. IGPM-report, RWTH Aachen, in preparation

[Vos02] Voß, A.: Flows in Fluids with Nonconvex Equation of State. PhD Thesis, RWTH Aachen, in preparation (2003)

7 Figures

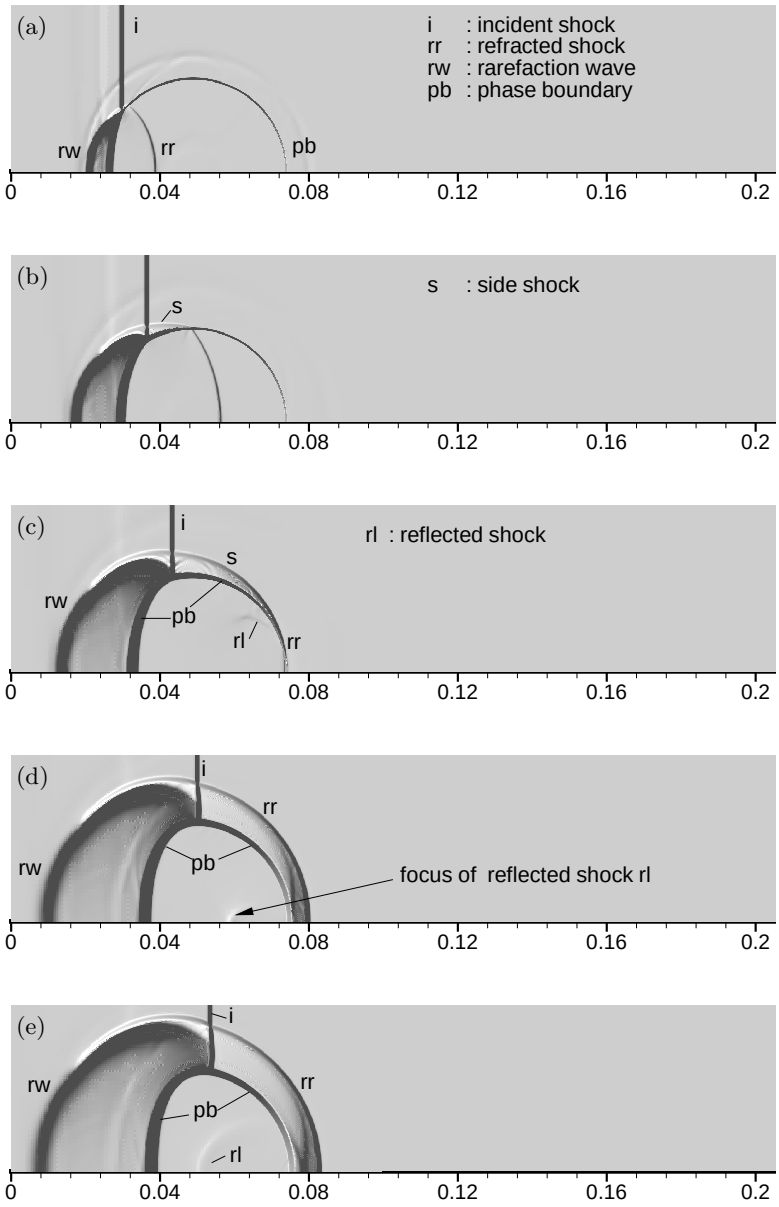

Fig. 4. Shock bubble (helium) interaction, (a)-(e): density gradients

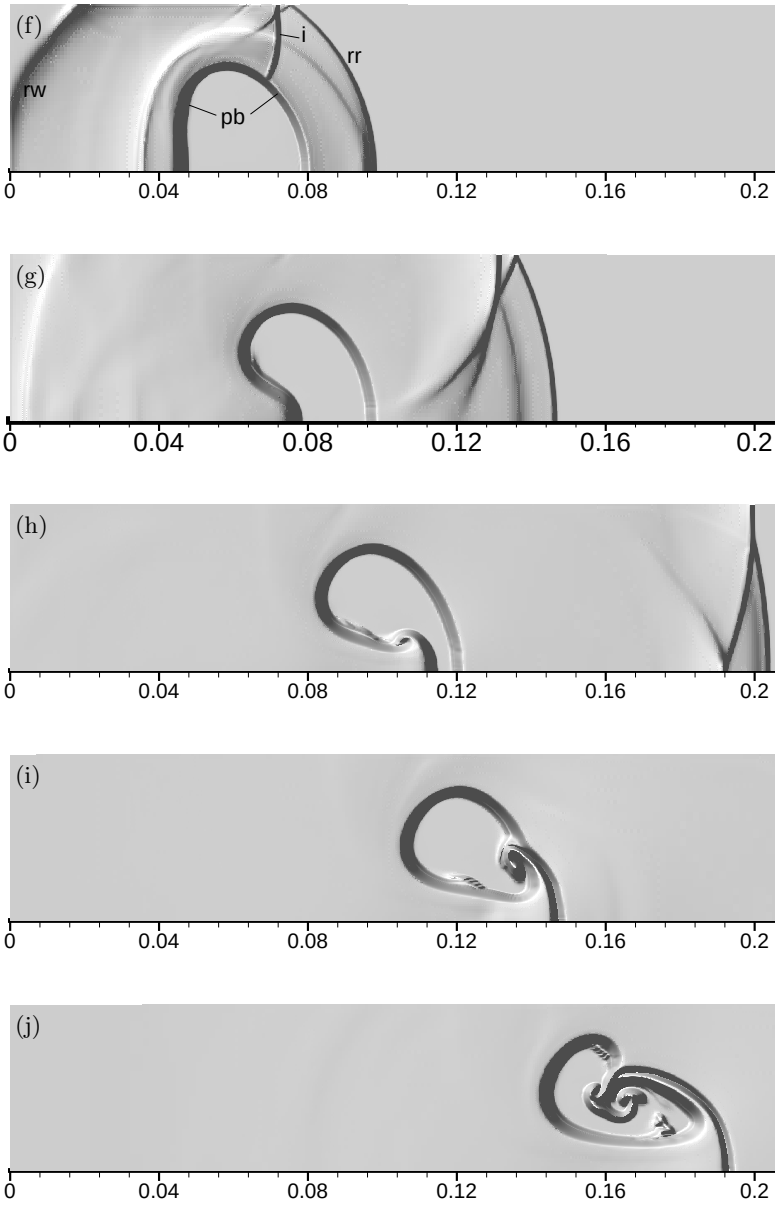

Fig. 4. Shock bubble (helium) interaction, (f)-(j): density gradients

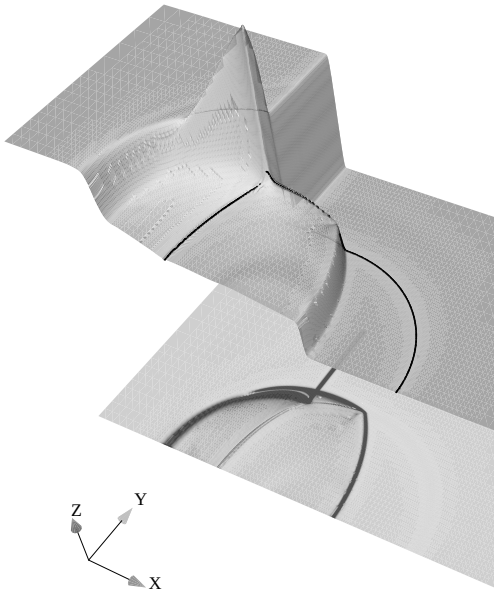

(a)

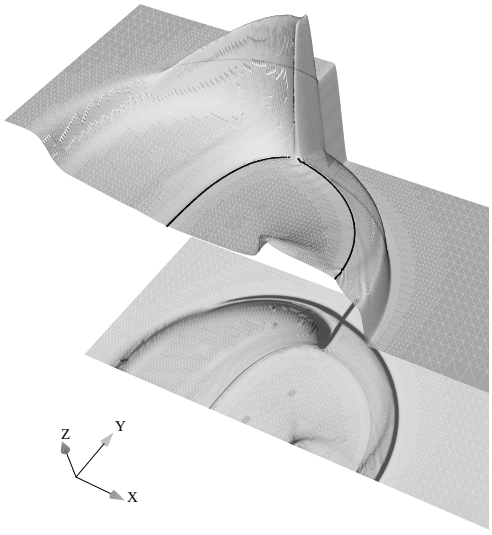

(b)

Fig. 5. x-y-plane: pressure gradients, z-axis: Pressure over x-y-plane with phase boundary marked as a black, solid line

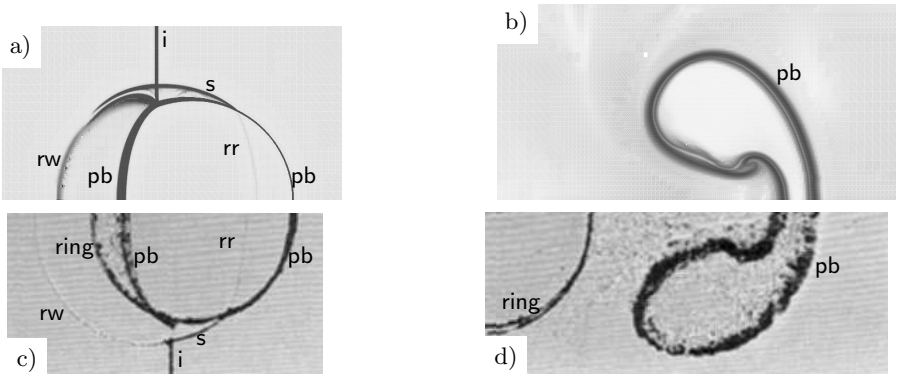

Fig. 6. Comparison between numerics (a,b) and experiment (c,d) for helium bubble in air. Experimental pictures scanned from [HS87]. The ring is part of the experimental setup. For the indices at the waves, see Fig. 4.

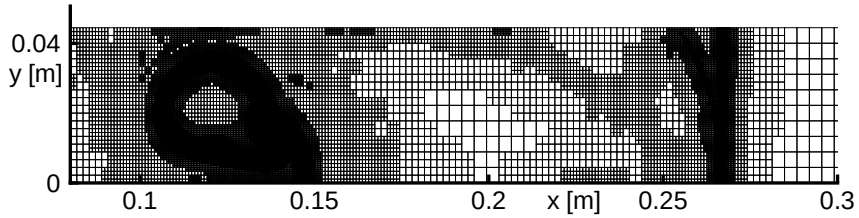

(a) Resolution of bubble (left) and shock (right).

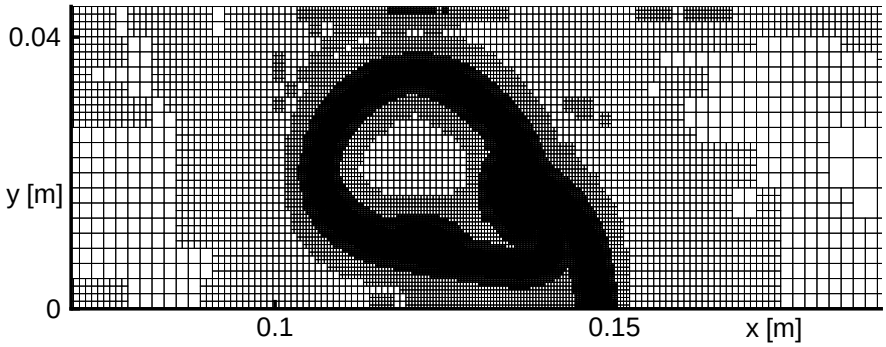

(b) Grid resolution in the bubble region.

Fig. 7. Parts of adapted mesh corresponding to Fig. 4(i)

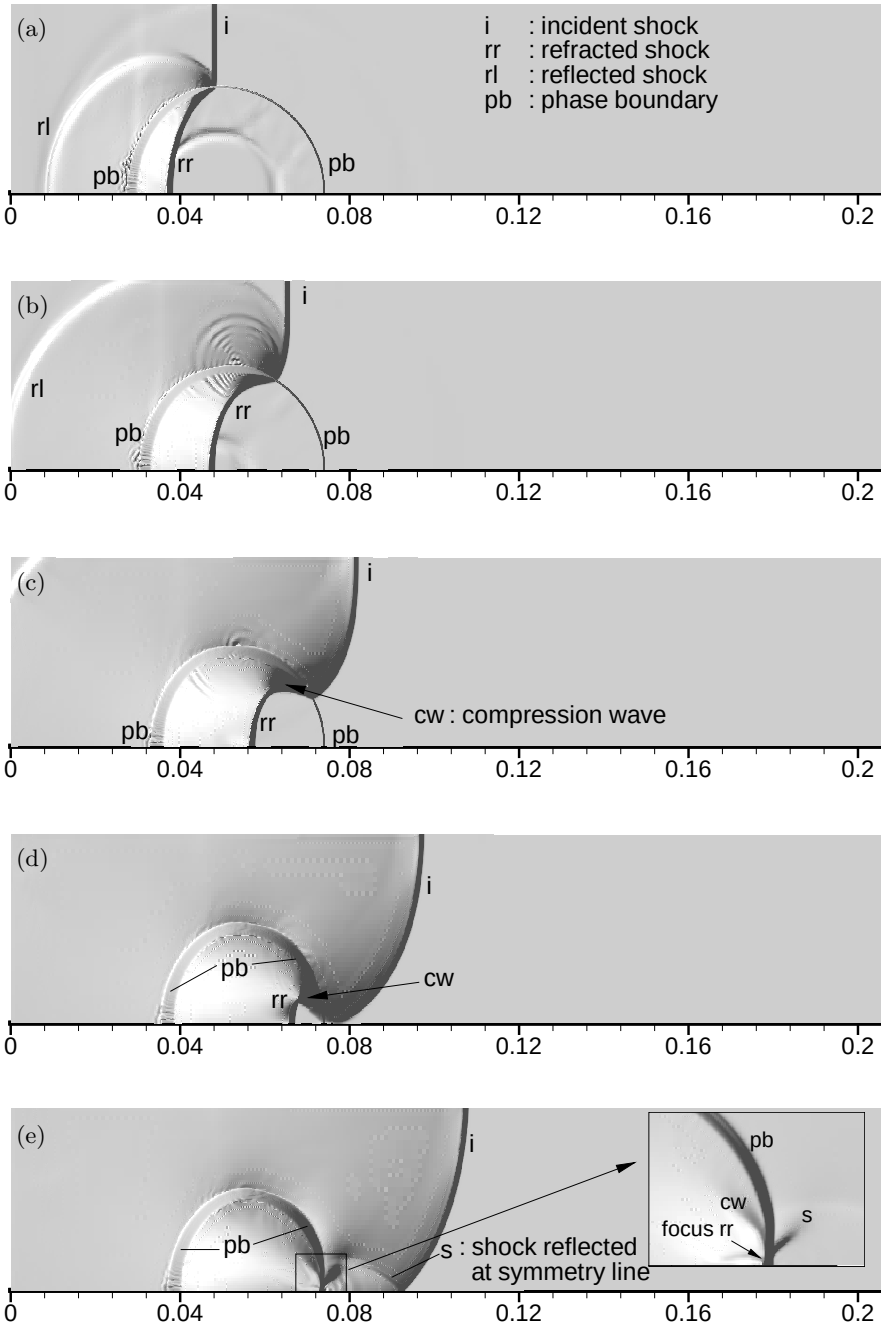

Fig. 8. Shock bubble (R22) interaction, (a)-(e): density gradients

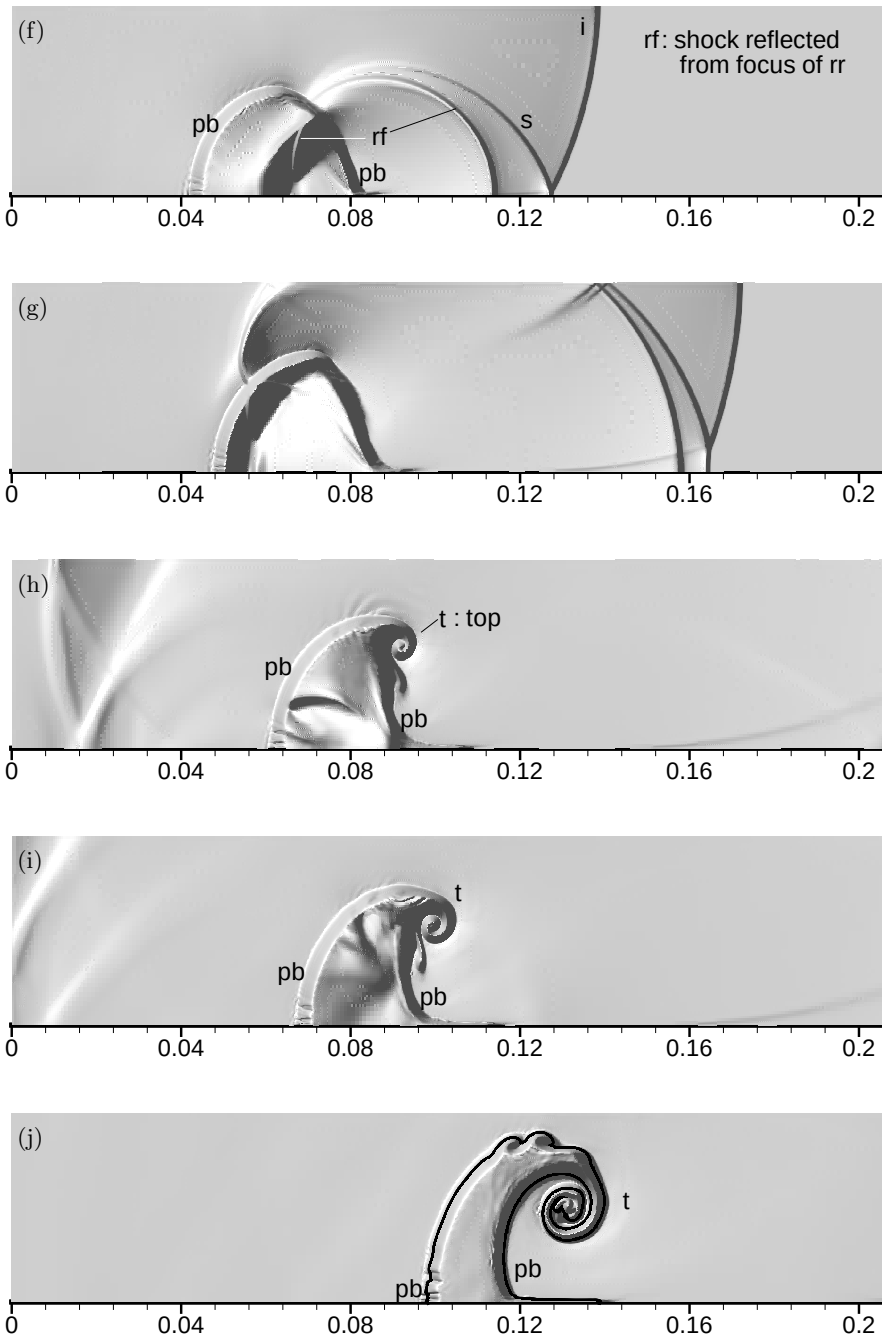

Fig. 8. Shock bubble (R22) interaction, (f)-(j): density gradients

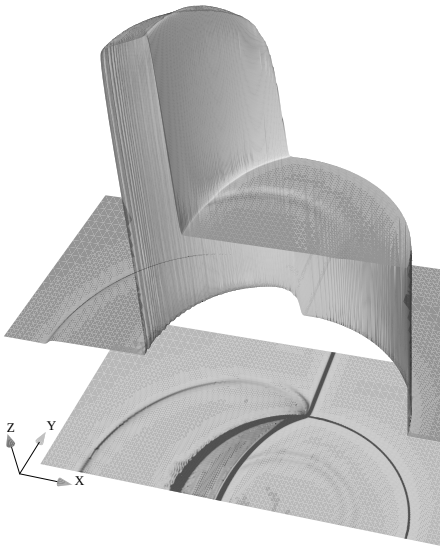

(a) x-y-plane: density gradients, z-axis: density over x-y-plane

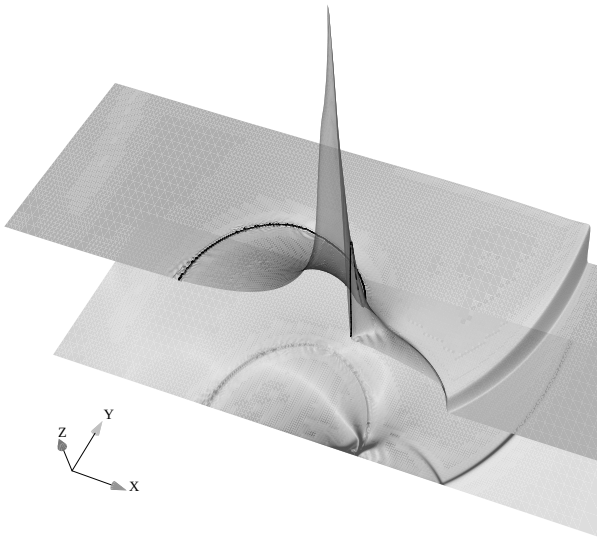

(b) x-y-plane: pressure gradients, z-axis: pressure over x-y-plane

Fig. 9.

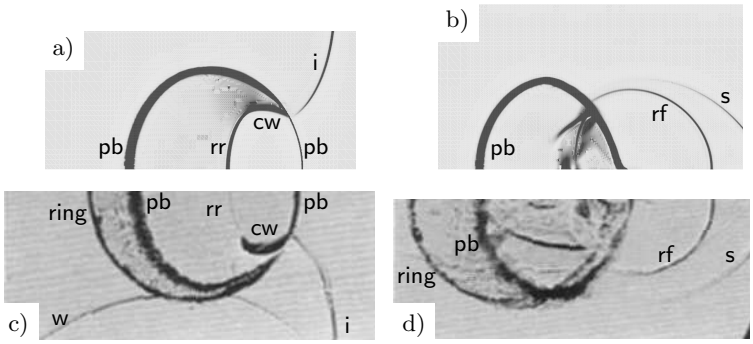

Fig. 10. Comparison between numerics (a,b) and experiment (c,d) for R22 bubble in air. Experimental pictures scanned from [HS87]. The ring is part of the experimental setup. For the indices at the waves, see Fig. 8.

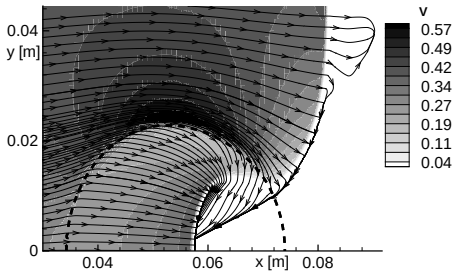

Fig. 11. Absolute value of velocity with integral-curves for v_x and v_y (arrows) and phase boundary ($\phi = 0$-level) as a black dashed line.

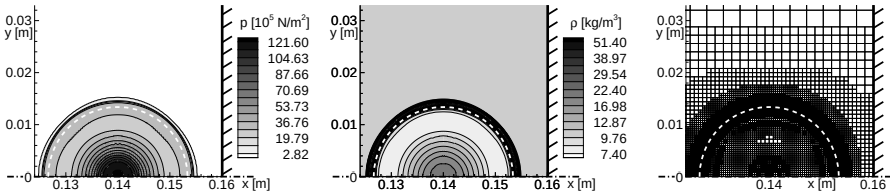

(a) pressure (b) density (c) grid

Fig. 12. $t = 7.0\mu$s, $\phi = 0$ white dashed line

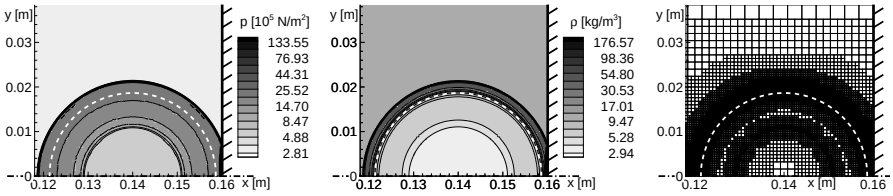

(a) pressure (b) density (c) grid

Fig. 13. $t = 18.53\mu$s, $\phi = 0$ white dashed line

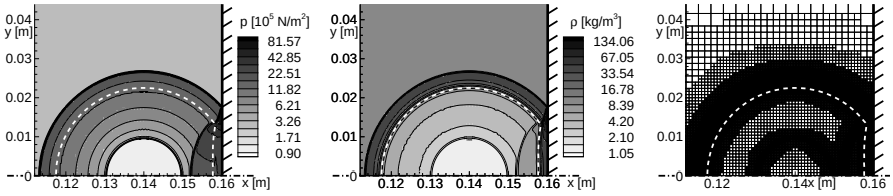

(a) pressure (b) density (c) grid

Fig. 14. $t = 29.00\mu$s, $\phi = 0$ white dashed line

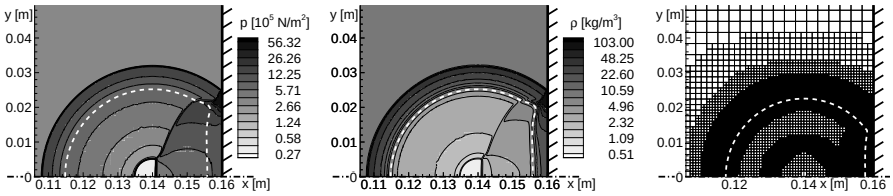

(a) pressure (b) density (c) grid

Fig. 15. $t = 40.00\mu$s, $\phi = 0$ white dashed line

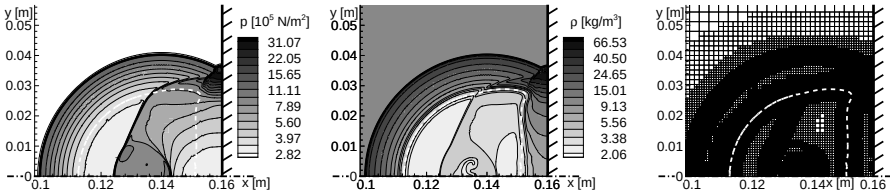

(a) pressure (b) density (c) grid

Fig. 16. $t = 59.99\mu$s, $\phi = 0$ white dashed line

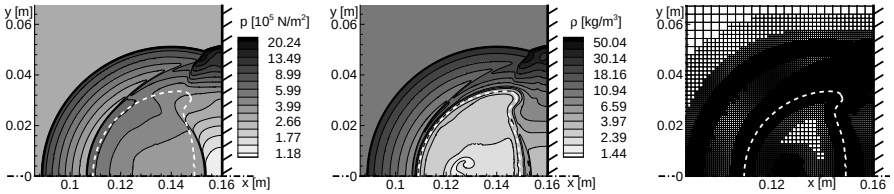

(a) pressure (b) density (c) grid

Fig. 17. $t = 90.01\mu$s, $\phi = 0$ white dashed line

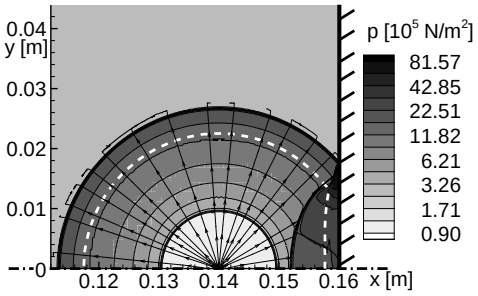

Fig. 18. Integral-curves

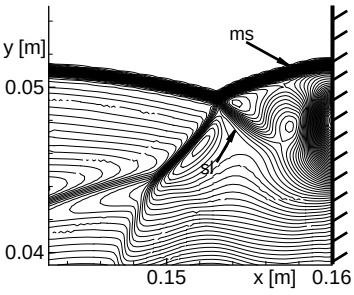

Fig. 19. Isolines of Mach number; mach stem (ms), slipline (sl)

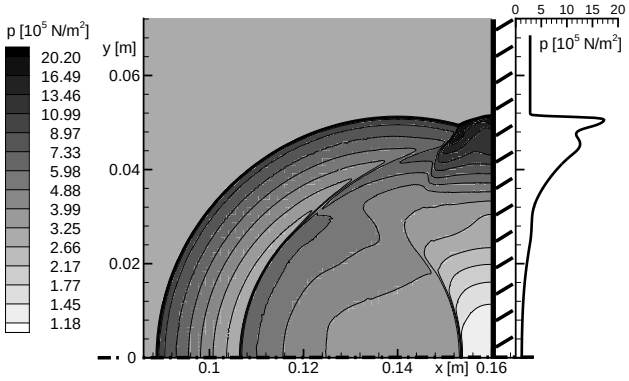

Fig. 20. Pressure distribution at wall

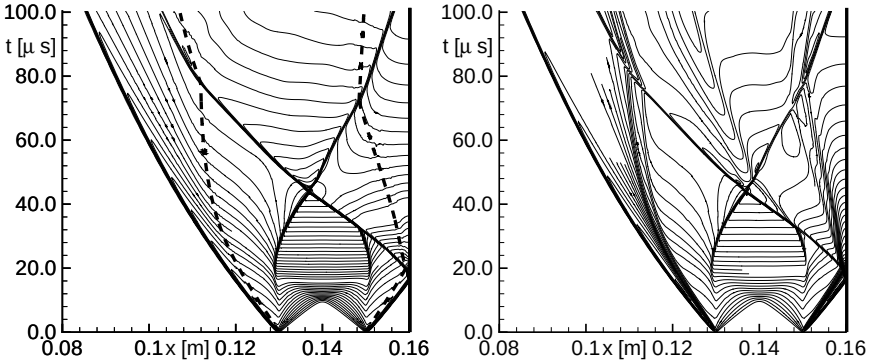

(a) Pressure isolines with $\phi = 0$ as black dashed line

(b) Density isolines

Fig. 21. Wave dynamic at x-axis for all computed time steps.